








Ab initio study of alkali-metal-based bismuth selenides ($ABiSe_2$; $A = K, Na$) for photovoltaic and thermoelectric applicationsSimeon A. Abolade ^{1,*}, Shittu B. Akinpelu ², David O. Obada ^{1,3}, Syam Kumar R ^{1,2}, Fedwa El-Mellouhi ⁴, Stefano Sanvito ⁵ and Akinlolu Akande ^{1,2,†}¹Centre for Mathematical Modelling and Intelligent Systems for Health and Environment (MISHE), Atlantic Technological University, Ash Lane, Ballytivnan, Sligo F91 YW50, Ireland²Modelling & Computation for Health And Society (MOCHAS), Atlantic Technological University, Ash Lane, Ballytivnan, Sligo F91 YW50, Ireland³Department of Mechanical Engineering, and Africa Centre of Excellence on New Pedagogies in Engineering Education, Ahmadu Bello University, Zaria 810222, Nigeria⁴Qatar Environment and Energy Research Institute, Hamad Bin Khalifa University, P.O. Box 34110, Doha, Qatar⁵School of Physics, AMBER and CRANN Institute, Trinity College, Dublin 2, Ireland

(Received 8 May 2023; accepted 18 December 2023; published 29 January 2024)

The structural, electronic, mechanical, and thermoelectric properties of alkali-metal-based bismuth selenides ($ABiSe_2$; $A = Na, K$) are investigated using a combination of *ab initio* density functional theory and semiclassical Boltzmann transport theory. The computed lattice constants are in close agreement with experimental results obtained from the Crystallography Open Database. The calculation of the phonon dispersion, elastic tensor, and formation energy confirm that both compounds are dynamically, mechanically, and thermodynamically stable. The band gaps of $KBiSe_2$ and $NaBiSe_2$ are indirect, and their room-temperature values computed at the HSE06 level including spin-orbit coupling (SOC) are 1.20 and 1.13 eV, respectively. SOC interactions impact the band gaps of these compounds which in turn influence the optical and thermoelectric properties, respectively. The absorption coefficients and figure-of-merit values obtained from optical and thermoelectric calculations suggest these materials as potential candidates for photovoltaic and thermoelectric applications.

DOI: [10.1103/PhysRevMaterials.8.015404](https://doi.org/10.1103/PhysRevMaterials.8.015404)**I. INTRODUCTION**

The constant growth in world population and widespread use of energy-demanding technologies are leading to a continuously increasing demand for energy, which is difficult to meet with available energy resources. As a result, presently, there is an acute interest in renewable energy production and management, through the development of solar cells and thermoelectric devices [1,2]. Solar cells built from hybrid organic-inorganic perovskites have recently achieved efficiencies of >25%, and they are currently considered one of the top candidate materials for photovoltaic technology [3]. Among the various options, formamidinium lead triiodide ($FAPbI_3$) is now identified as one of the frontrunner compounds, having a 25.2% power conversion efficiency and stable operation for a long period [4]. However, the presence of lead in these highly efficient perovskites remains a major concern. This is inextricably linked to air instability, humidity sensitivity, toxicity, and the health risks associated with Pb [5,6]. Several strategies have been suggested to overcome this drawback, including synthesizing alternative compounds by looking out for elements to replace Pb ions. For instance, attempts have been made toward substituting Pb with Sn, but Sn-based com-

pounds have been found to be unstable due to the ease of oxidation of the Sn^{2+} ion [7].

Another viable option is to use bismuth, which has an outer $6s^2$ lone pair like Pb and is not harmful [8]. Bi is also a heavy group-V element with significant spin-orbit coupling (SOC), which typically influences important features of the band structure [9]. Interestingly, the Bi ionic radius, electronegativity, and valence electronic shell are comparable with that of Pb [10,11]. Bi-based oxides have been reported to have the ability to absorb light near the infrared region since the Bi 6s shell can hybridize with O 2p orbitals belonging to the chalcogen group. This hybridization can form an advantageous hybridized valence band as well as narrow band gap suitable for light absorption [12]. Bi is also a stable, inexpensive, easily functionalized element with good electrical and diamagnetic characteristics. Therefore, it becomes an intriguing element for the development of compounds for industrial applications. Because of these distinctive properties, bismuth-containing compounds, particularly those with alkali metals, and chalcogens have lately been explored for photovoltaic and thermoelectric applications [13]. For instance, the presence of chalcogen elements such as O, S, Se, and Te typically results in structural and thermodynamic stability [14], so it is not surprising to see several recent experimental investigations on this class of compounds appearing.

For example, Yang *et al.* [15] synthesized and characterized chalcogenide compounds with the $ABiX_2$ formula ($A = Na, K$,

*Corresponding author: simeon.abolade@research.atu.ie†Corresponding author: akinlolu.akande@atu.ie

or Cs, and $X = \text{S}$ or Se) and found that these systems possess outstanding stability in air and strong absorption in the visible to near-infrared region. Rosales *et al.* [16] also reported that $APnX_2$ ($A = \text{Na}$, $Pn = \text{Bi}$, $X = \text{S}$ or Se) semiconductors exhibit intermediate band gaps within the 1.20–1.45 eV range, namely, in an optimal solar cell energy window. Theoretical studies also exist for some materials of this class, including the NaAX_2 ($A = \text{As}$, Sb , Bi ; $X = \text{S}$, Se , Te) monoclinic structures investigated by Khare *et al.* [13]. Their findings indicated that three of these compounds are dynamically stable and exhibit strong absorption values ranging from 10^4 to 10^5 cm^{-1} in the visible-ultraviolet range. Kumar R. *et al.* [17] performed a theoretical investigation of ABiX_2 and ABiX_3 ($A = \text{Na}$, K and $X = \text{O}$, S) and discovered that NaBiO_2 and KBiO_2 have direct band gaps and absorb light in the visible spectrum. It was also reported that these systems are mechanically stable, providing an overall good outlook for the use of bismuth-based chalcogenide compounds in photovoltaic applications.

When designing a thermoelectric compound, one must maximize the Seebeck coefficient S and the electrical conductivity σ as well as minimize the thermal conductivity k . The power factor $P = S^2\sigma$ and the figure of merit $ZT = \sigma S^2 T/k$, which depends on these thermoelectric quantities, help in determining the performance of a device. Several theoretical studies have been conducted investigating the thermoelectric performance and ZT of chalcogenide compounds. Mohyedin *et al.* [18] studied Bi_2Te_3 using the local density approximation parametrization of density functional theory (DFT) including SOC. Their findings demonstrate that eliminating the magnetic component of the material, which required SOC, provides analytical insight on how to improve the thermoelectric performance. Ternary chalcogenides with formula ABX_2 , where the A and B sites host a metal and the X site a chalcogen ion, have also been reported to possess promising thermoelectric features [19]. Lee *et al.* [20] reported A_2SbSe_8 ($A = \text{K}$, Rb , and Cs) to be an interesting class of materials for thermoelectric applications based on a calculated Seebeck coefficient and power factor greater than those of Bi_2Te_3 and PbTe , which are commonly known thermoelectric materials. According to Tabeti *et al.* [21], AgBiS_2 shows a figure of merit increasing with doping and reaching maxima of ~ 0.95 and 0.85 for a carrier concentration of $2 \times 10^{19} \text{ cm}^{-3}$ in p - and n -type doping conditions, respectively. Furthermore, systems belonging to the group I-V-VI₂ family (where I = Cu or Ag, V = Sb or Bi, and VI = S, Se, and Te) have also been mentioned as promising thermoelectric materials due to their low thermal conductivity [22,23]. In addition, inorganic thermoelectric materials have been reported to simultaneously achieve high thermoelectric performance and flexibility with a good potential in portable/wearable electronic applications [24]. For instance, Zhu *et al.* [25] reported that Bi_2Te_3 shows noticeable advancements as wearable electronics because of its good thermoelectric performance around room temperature. Also, Qiao *et al.* [26] doped Te on Bi_2Te_3 using a grain boundary diffusion route. The thermal conductivity was observed to effectively reduce without minimizing the electrical conductivity, and a ZT value of 0.67 was obtained at room temperature.

Motivated by these fascinating findings concerning bismuth-based chalcogenide materials, in this work, we

present a theoretical study of alkali-metal-based Bi selenides with ABiSe_2 formula, where $A = \text{Na}$, K . Only a few preliminary investigations are available in the literature for this class. Thus, structural, electronic, mechanical, thermodynamic, dynamical, and transport properties are here explored. We consider the experimentally synthesized trigonal ($R\bar{3}m$ space group) structure [27], from the Crystallography Open Database, and we conduct our study using various levels of DFT together with the semiclassical Boltzmann theory for transport.

II. COMPUTATIONAL METHODS

All calculations are performed with projector augmented-wave DFT as implemented in VASP [28,29]. The standard Perdew-Burke-Ernzerhof (PBE) parameterization of the generalized gradient approximation (GGA) is used as the exchange-correlation functional [30,31]. The KBiSe_2 structure considered in this work is obtained from the Crystallography Open Database, while NaBiSe_2 is modeled by exchanging K with Na at the corresponding cation site. An energy cutoff of 350 eV is used in the expansion of the plane-wave, together with a Gaussian smearing of 0.1 eV and a $6 \times 6 \times 1$ Γ -centered k -point mesh (see Fig. S4 in the Supplemental Material [32]). To account for the weak dispersive forces, Grimme DFT-D3 (BJ) van der Waals (vdW) [33,34] corrections are included. SOC is considered when computing the electronic properties calculations because of the existence of heavy atoms but not during the geometry relaxation. The inability of the GGA to return good estimates of the band gap is mitigated by performing further calculations on the relaxed structures at the level of the Heyd-Scuseria-Ernzerhof (HSE06) hybrid functional [35]. Furthermore, *ab initio* molecular dynamics (MD) simulations are carried out using the canonical ensemble at constant temperature and volume (NVT ensemble) to investigate the effects of temperature on the band gaps. The integration of the bulk Brillouin zone is carried out with a Γ -centered k -point mesh for all DFT-MD simulations within a $3 \times 3 \times 1$ supercell model. The ionic positions of the reported experimental structure (KBiSe_2) are updated by varying the temperature from 100 to 500 K via MD calculations to obtain initial structures at different temperatures with an interval of 100 K. These temperatures are maintained with a Nosé-Hoover thermostat [36,37]. The system is thermalized using a time step of 4 fs until equilibrium is achieved (see Fig. S6 in the Supplemental Material [32]). Then the total MD simulation time is 20 ps and comprises 5000 steps at a 4 fs resolution. Electronic band gap calculations are then carried out on the output structures obtained at different temperatures.

The dynamical stability of the compounds studied is investigated by computing their phonon dispersion curves in the harmonic approximation [38]. By using a $3 \times 3 \times 1$ supercell and a $2 \times 2 \times 1$ k -grid mesh, the Hessian matrix is computed with the finite displacement method [39] at zero temperature. Then the PHONOPY code [40] is used to compute the harmonic phonon frequencies along the high-symmetry pathway in the Brillouin zone.

The thermodynamic stability of the compounds is assessed by computing the formation and decomposition energy with respect to their constituent elements as illustrated in Eqs. (1)–

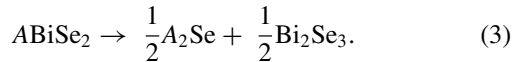
TABLE I. Calculated lattice parameters ($a = b, c$), angles ($\alpha = \beta = 90, \gamma = 120$), unit-cell volume V , and number of atoms per unit cell N_a , for KBiSe_2 and NaBiSe_2 , in their trigonal crystal structure (space group $R\text{-}3m$). The percentage differences between calculated and experimental data are reported in the bracket.

Compound	Values from	N_a	a (Å)	c (Å)	V (Å ³)
KBiSe_2	Experiment [27]	12	4.26	23.03	362.68
	This work	12	4.24 (-0.47%)	22.87 (-0.70%)	356.73 (-1.64%)
NaBiSe_2	This work	12	4.17	20.76	311.90

(3). The energies of the reactant compounds and elemental phases are obtained from the Materials Project database and reoptimized to yield a consistent ground-state energy. The formation energy E_{form} effectively measures the bond energy, while the decomposition energy ΔE_d establishes whether the ternary phase is unstable against binary decomposition:

$$E_{\text{form}} = E(\text{ABiSe}_2) - E(\text{A}) - E(\text{Bi}) - 2E(\text{Se}), \quad (1)$$

$$\Delta E_d = \left[\sum_i c_i E_i^{\text{binary}} / N_i \right] - \frac{E^{\text{ternary}}}{N}, \quad (2)$$



In the formulas above, $A = \text{Na}$ or K , while E^{ternary} and E_i^{binary} represent the ground-state energy per formula unit of the binary and ternary compounds, respectively. Here, N and N_i are total number per formula unit of the atom of the i th binary and ternary systems, while c_i is the fractional coefficient required to balance the chemical reaction. The specific decomposition pathway of the studied compounds was obtained from the KBiSe_2 convex hull construction reported in Ref. [27]. A similar decomposition pathway is adopted for NaBiSe_2 .

The dielectric tensor is computed from the DFT band structure within the random phase approximation, and the real ϵ_1 and imaginary ϵ_2 parts of the static dielectric constant are related through the Kramer-Kronig relation. The absorption coefficients $\alpha(\omega)$ for both compounds are evaluated through the relation [41,42]:

$$\alpha(\omega) = \sqrt{2\omega} \sqrt{\sqrt{\epsilon_1^2(\omega) + \epsilon_2^2(\omega)} - \epsilon_1(\omega)},$$

where $\epsilon_1(\omega)$ and $\epsilon_2(\omega)$ are the frequency-dependent real and imaginary parts of the dielectric function, respectively.

An assessment of the mechanical stability of the materials is carried out by using the Born stability criteria, which encompass a collection of conditions that are necessary and sufficient to establish the stability of a given material in its unstressed state. These conditions are specific to different structures. For the trigonal lattice considered in this work, the Born stability criteria is defined as $C_{11} > |C_{12}|$, $C_{44} > 0$, $C_{13}^2 < \frac{1}{2}C_{33}(C_{11} + C_{12})$, and $C_{14}^2 < \frac{1}{2}C_{44}(C_{11} - C_{12}) \equiv C_{44}C_{66}$ [43,44].

Finally, the thermoelectric transport coefficients are calculated by solving the semiclassical Boltzmann transport equation within the constant relaxation time approximation as implemented in the BoltzTraP code [45] and a denser k -mesh of $24 \times 24 \times 4$. It is worth noting that the electronic thermal conductivity k_e is usually larger than the lattice thermal conductivity k_l for this class of compounds. Indeed, for

a complete evaluation of the full thermoelectric properties, the inclusion of the lattice thermal conductivity would be desirable, as it may alter the resulting figure of merit [46]. However, this is outside the capability of the BoltzTraP code, which only computes the electronic thermal conductivity, and such an analysis is postponed to future work. In this way, we obtain the Seebeck coefficient, power factor, and figure of merit with respect to the chemical potential and carrier concentration.

III. RESULTS AND DISCUSSIONS

A. Structural properties

The calculated lattice parameters, unit-cell volumes, and space group of KBiSe_2 and NaBiSe_2 are summarized in Table I, while their related ball-and-stick polyhedral structures are displayed in Fig. 1. After geometric optimization, it is observed that the two compounds retain the trigonal $R\text{-}3m$ structure. For KBiSe_2 , whose initial geometry was taken from the Crystallography Open Database, the lattice parameters of the optimized structure are in very good agreement with the experimental lattice parameters [27]. In this case, GGA underestimates the lattice vectors by <1% and the unit-cell volume by <2%, as expected by the gradient approximation of DFT. This result is comparable with the theoretically obtained lattice parameters ($a = b = 4.31$ Å and $c = 23.29$ Å) found in the Automatic-FLOW (AFLOW) database [47]. As seen in Fig. 1, the trivalent Bi cations are bonded to six Se atoms in octahedral local coordination, and the same for K cations. The overall molecular geometry of BiSe_6 has edge and face sharing with KSe_6 .

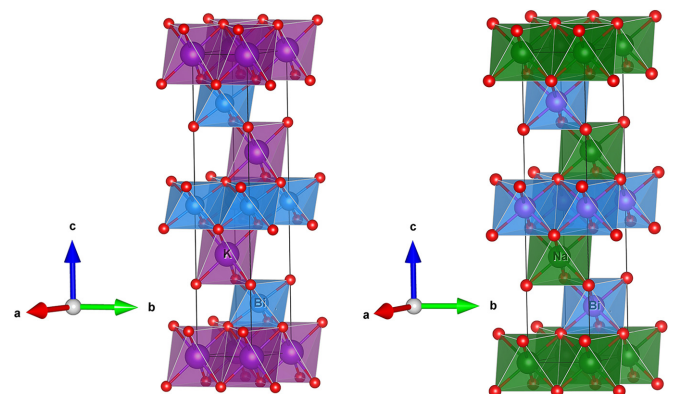


FIG. 1. The crystal structure of KBiSe_2 (left) and NaBiSe_2 (right). Color code: K = purple, Na = green, Bi = blue, and Se = red. The initial NaBiSe_2 geometry is constructed by the exchange of K with Na in the optimized KBiSe_2 structure.

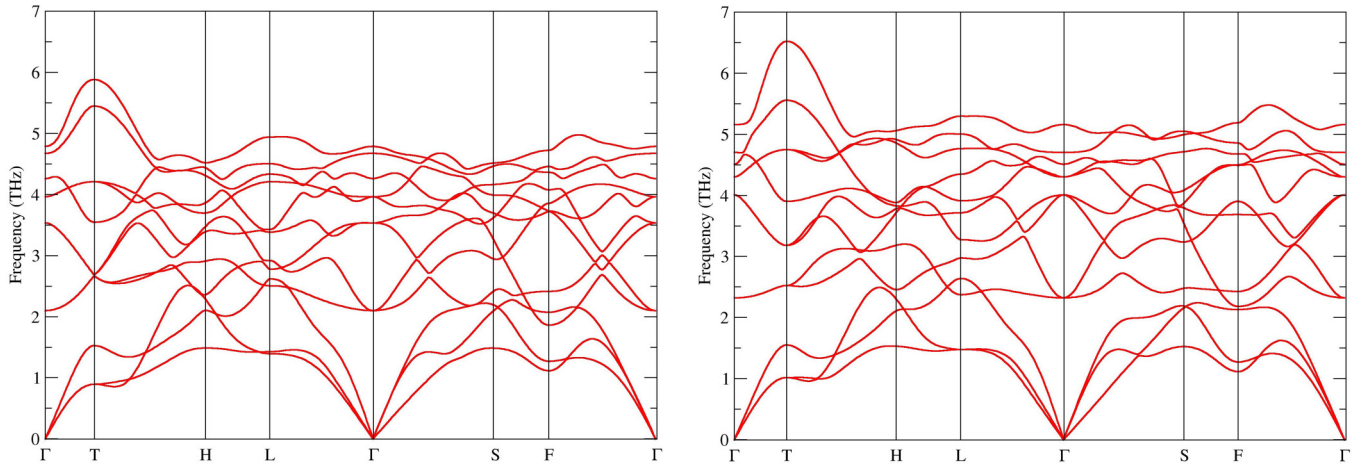


FIG. 2. Phonon dispersion curves of KBiSe_2 (left) and NaBiSe_2 (right), computed with the PBE functional and the harmonic approximation at 0 K.

NaBiSe_2 is initially constructed by replacing K with Na at the corresponding A cation site, and it is also relaxed to a trigonal structure. The lattice constants obtained after optimization are also comparable with $a = b = 4.20 \text{ \AA}$ and $c = 21.15 \text{ \AA}$ found in the Materials Project as well as $a = b = 4.24 \text{ \AA}$ and $c = 21.27 \text{ \AA}$ reported in the AFLOW database [48,49], respectively. It is observed that the volume and lattice constants decrease upon exchanging K with Na, reflecting the smaller ionic radius and difference in electronegativity of Na compared with those of K. The local coordination and octahedra structure are identical in the two compounds.

B. Dynamical and thermodynamic properties

The phonon dispersion is calculated to investigate the dynamical stability of the two structures, and the results are summarized in Fig. 2 (PBE phonon band structure). Clearly, no imaginary phonon branches are found, indicating that both compounds are dynamically stable at zero temperature. As expected, the phonon band structures of KBiSe_2 and NaBiSe_2 are rather similar, again reflecting the tight structural and electronic similarity of the two compounds.

The thermodynamic stability of KBiSe_2 and NaBiSe_2 is determined by computing both the formation E_{form} and decomposition ΔE_d energies, as described by Eqs. (1)–(3).

In both cases, the prototypes of competing stable phases are taken from the Materials Project dataset [48] and are PBE relaxed. We find that, for both compounds, E_{form} is negative, namely, it is -3.31 eV/f.u for KBiSe_2 and -3.07 eV/f.u for NaBiSe_2 , indicating that these compounds are thermodynamically stable against decomposition along their constituent elementary references. In addition, the formation energies obtained are commensurate with -3.83 eV/f.u reported for KBiSe_2 and -3.78 eV/f.u reported for NaBiSe_2 in the AFLOW and Materials Project databases [47,48]. Here, E_{form} only gives a measure of the total bond energy of a material but says little about the actual stability. To further investigate the stability of these systems, Eq. (2) is used to calculate the decomposition energy, a quantity that describes the energetic gain of forming the ternary structure against the most favorable possible binary decomposition channel. According to the definition, $\Delta E_d > 0$ implies that no energetically favorable decomposition reaction exists, while $\Delta E_d < 0$ shows that the $\text{ABiSe}_2 \rightarrow \frac{1}{2}\text{A}_2\text{Se} + \frac{1}{2}\text{Bi}_2\text{Se}_3$ decomposition path has a lower energy than the ternary material under consideration. The decomposition path chosen for KBiSe_2 is that suggested by McClain *et al.* [27], while that for NaBiSe_2 is obtained by exchanging K with Na. In both cases, $\Delta E_d > 0$ with values 1.93 and 1.89 eV/f.u. respectively, for KBiSe_2 and NaBiSe_2 , indicating that both phases are likely to be stable.

TABLE II. Calculated electronic band gaps E_g at different level of theory and available experimental results. The computed electronic band gaps of NaBiSe_2 and KBiSe_2 at the PBE, HSE06, PBE+SOC, and HSE06+SOC levels are listed. In addition, estimates of the PBE+SOC and HSE06+SOC band gaps at 300 K are presented. Finally, available experimental and theoretical data for the two compounds are included in the last two columns.

Compounds	Band gaps E_g (eV)							
							Reported	
	PBE	PBE+SOC	HSE06	HSE06+SOC	PBE+SOC at 300 K	HSE06+SOC at 300 K	Experimental	Theoretical
KBiSe_2	1.26	0.83	1.96	1.38	0.68	1.20	1.09 [27] ^{trigonal} 1.40 [15] ^{cubic}	1.12 [27] ^{trigonal}
NaBiSe_2	1.25	0.80	1.93	1.31	0.64	1.13	1.31 [15] ^{cubic}	1.23 [13] ^{monoclinic}

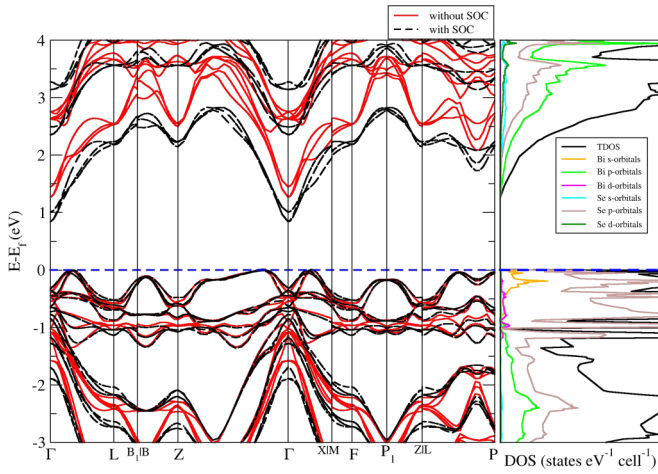


FIG. 3. PBE-calculated energy band structure and partial density of states (PDOS) of KBiSe_2 . The compound is found to be an indirect band-gap semiconductor with the valence band maximum (VBM) located along the Γ -to- L and Z -to- Γ lines, while the conduction band minimum (CBM) lies at Γ . The black-dashed and red lines are bands computed with and without the inclusion of spin-orbit coupling (SOC), respectively. The Fermi level is placed at the VBM and set to zero.

C. Electronic properties

Table II shows the computed band gaps for the trigonal structure compared with existing data (both theoretical and experimental). Note that, in the literature, one can also find results for cubic and monoclinic phases, which are not investigated here. Both KBiSe_2 and NaBiSe_2 possess indirect band gaps, with the valence band maximum (VBM) located, respectively, along the Γ -to- L and Z -to- Γ lines, while the conduction band minimum (CBM) is at Γ (Figs. 3 and 4). Interestingly, the valence band has a bandwidth value of 0.49 eV for KBiSe_2 and 0.74 eV for NaBiSe_2 , while the conduction band is more dispersive with a bandwidth of 2.16 eV for KBiSe_2 and 1.62 eV for NaBiSe_2 . The PBE functional returns a KBiSe_2 band gap of 1.26 eV, which is unusually larger than the experimental optical band gap of 1.09 eV reported by McClain *et al.* [27]. In contrast, HSE06, which usually does a good job at predicting band gaps, gives us an estimate of 1.96 eV, meaning that the gap is significantly larger than the observed one (see Fig. S1 in the Supplemental Material [32] for the HSE06 band structures), although the general shape of the band structure is not changed significantly from the PBE ones. Such an overestimation has previously been reported by Qu *et al.* [49] for the same trigonal structure but a different chemical composition, namely, for KBiS_2 . Two effects may play a role in such anomalies in the band gap prediction, namely, temperature (the experimental band gap in Ref. [27] was measured at 300 K) and SOC, these are now considered in detail.

Temperature affects the band gap since volume expansion and atomic vibration effectively changes the structure [50]. To capture these effects, we have performed *ab initio* MD simulations and evaluated the band gap of KBiSe_2 as a function of temperature (we compute the average band gap for several un-

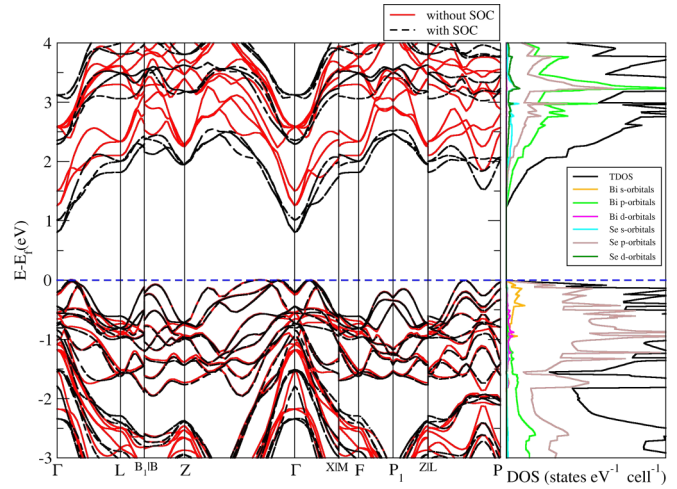


FIG. 4. PBE-calculated energy band structure and partial density of states (PDOS) of NaBiSe_2 . The compound is found to be an indirect band-gap semiconductor with the valence band maximum (VBM) located along the Γ -to- L and Z -to- Γ lines, while the conduction band minimum (CBM) lies at Γ . The black-dashed and red lines are bands computed with and without the inclusion of spin-orbit coupling (SOC), respectively. The Fermi level is placed at the VBM and set to zero.

correlated snapshots along the MD trajectory). Results for the band gap using the PBE functional are reported in Fig. 5 (see also Fig. S5 in the Supplemental Material [32] for snapshots of PBE-calculated band structures of KBiSe_2 at the temperature range of 100–500 K), where one can see that the average gap at 300 K is now 1.05 ± 0.05 eV, namely, there is ~ 0.20 eV reduction from the $T = 0$ value. Furthermore, the inclusion of SOC has the effect of shrinking the band gap since both the conduction and valence bands are characterized by orbital contributions originating from heavy Bi and Se. Here, SOC inclusion brings the PBE gap to 0.83 eV and the HSE06 one to 1.38 eV. Finally, the two effects can be combined under the

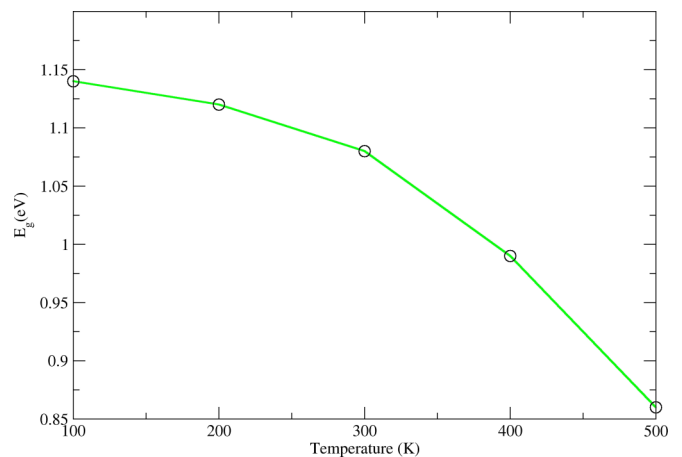


FIG. 5. PBE-calculated band gap of KBiSe_2 as a function of temperature in the 100–500 K range. This is computed from the structure obtained through *ab initio* molecular dynamics (MD) simulations.

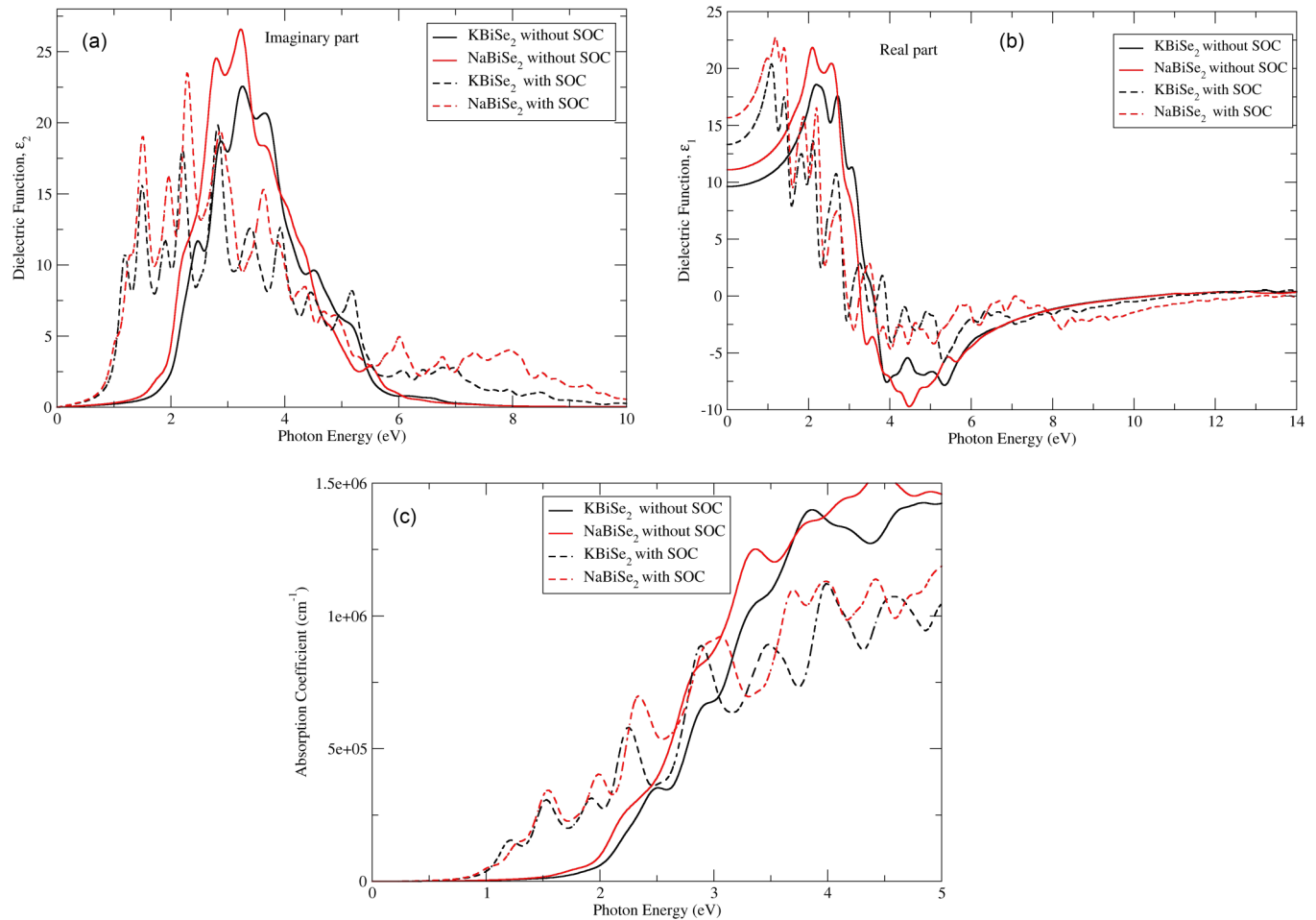


FIG. 6. The calculated PBE optical properties with and without SOC as a function of photon energy for KBiSe₂ and NaBiSe₂ (a) imaginary component of the dielectric function (b) real part of the dielectric function and (c) the absorption coefficient.

reasonable assumption that the temperature variation of the band gap depends little on SOC and on the DFT functional used. In this case, one can simply add to the SOC-included computed gap, the reduction observed for PBE when going from 0 to 300 K. This exercise returns final estimates of the 300 K band gap of 0.68 and 1.20 eV, respectively, for PBE and HSE06 (see Table II). As expected, PBE significantly underestimates the experimental value, while the HSE06 gap is rather close to the observed one.

In the case of NaBiSe₂, no experimental data are available in the literature for the trigonal phase, data are only available for the cubic one [15]. The observed gap is 1.31 eV, namely, it is almost identical to that of the cubic phase of KBiSe₂ (1.40 eV) [15]. HSE06 calculation including SOC returns a gap of 1.31 eV for the trigonal phase, which may reduce to ~ 1.13 eV if one applies the same temperature correction introduced for KBiSe₂. Hence, we can conclude that both materials investigated have band gaps ~ 1.20 eV regardless of the alkaline ion present. This is not unexpected since the valence and conduction bands are dominated by Bi and Se orbitals and the two compounds have the same crystal structure and only a slightly different volume. In fact, by observing the orbital-projected density of states of Figs. 3 and 4, we can conclude that, for both materials, the VBM is dominated by a mixture of Se-*p* and Bi-*s* orbitals, while the CBM has a

predominant Bi-*p* character. This electronic structure is very consistent with the +3 oxidation state of Bi.

D. Optical and dielectric properties

When studying solar cell materials, it is crucial to examine their optical properties, which are determined by their band gaps and dielectric functions. As light with a specific photon energy (wavelength) enters a material, its intensity reduces, and the absorption coefficient determines how far the light can penetrate before being absorbed. This information is vital, as it reveals the potential of the material to achieve optimal solar energy conversion [51]. The optical properties of the two compounds were calculated to determine their potential in optoelectronic and photovoltaic applications [52–54] using all 55 unoccupied bands. Figures 6(a) and 6(b) show the computed imaginary ϵ_2 and real ϵ_1 components of the frequency-dependent dielectric function. The material polarizability is related to ϵ_1 , while its absorptive activity is described by ϵ_2 , and both are computed at the PBE and PBE+SOC level. Raju and Thangavel [55] reported a significant reduction of the optical band gaps, up to 25%, of a related compound (CuBiSe₂) when SOC is included. This is noticed for compounds with heavy atoms as evident in this work, and

TABLE III. Independent components of the elastic tensor of KBiSe_2 and NaBiSe_2 in their trigonal structure.

Elastic constants	C_{11} (GPa)	C_{12} (GPa)	C_{13} (GPa)	C_{14} (GPa)	C_{33} (GPa)	C_{44} (GPa)
KBiSe_2	73.66	20.83	27.30	13.27	59.96	27.45
NaBiSe_2	85.64	25.61	25.61	11.65	57.31	28.61

a significant reduction of $\sim 40\%$ is present here in the optical band gaps of the absorption coefficient [see Fig. 6(c)].

From Fig. 6(a), we can observe a similar onset for NaBiSe_2 and KBiSe_2 , which reflects the similarity in their band gaps when PBE and PBE+SOC functionals are used. Upon the inclusion of SOC, a notable redshift in the edge of the imaginary part of the dielectric function is observed in contrast to the PBE result for both compounds. For instance, the first peaks in ϵ_2 are located at 2.48 eV (KBiSe_2) and 2.80 eV (NaBiSe_2) for the PBE functional, while those computed with SOC are found lower at 1.20 and 1.51 eV, respectively, for KBiSe_2 and NaBiSe_2 . Similar changes are found in the real part of the dielectric function, as shown in Fig. 6(b). Interestingly, both components of the dielectric function are higher for NaBiSe_2 than for KBiSe_2 , a difference that we attribute to the different cell volumes and electronegativity induced by the choice of alkaline ion. In general, for both compounds, the first peak in the dielectric function obtained by using the PBE functional appears within the visible region 1.62–3.11 eV [56], and this is mirrored by the computed absorption coefficient, with similar onset for both compounds [see Fig. 6(c)].

The absorption onset can be operationally defined as the energy where the absorption coefficient reaches a value of 10^5 cm^{-1} (Szymanski *et al.* [57]). Materials with an absorption onset comprising between 0.80 and 1.70 eV and bracketing peaks in the AM1.5 solar irradiance spectrum are considered suitable for solar cell applications [58]. The PBE-calculated absorption onsets for both materials are observed to be ~ 1.50 eV [Fig. 6(c)]. This value is slightly larger than the electronic band gaps, a difference that can be attributed to the difference between the direct and indirect band gaps [59]. In contrast, the PBE+SOC onsets are lower than the PBE only, with an absorption band energy of ~ 0.85 eV, comparable with the value of the PBE+SOC band gap. As noticed before, the use of the HSE06 functional and the inclusion of temperature effects returned an estimation of the band gap at ~ 1.20 eV. Since HSE06, in first approximation, simply shifts the bands, such an increase is expected to also carry on in the absorption coefficient. As such, we can conclude that the room-temperature absorption edge for these compounds is estimated at ~ 1.20 eV. Note, that our calculations do not consider possible excitonic effects, so that our estimated absorption edges are not inclusive of the exciton binding energy. These

are estimated to be $\sim 200\text{--}300$ meV, as reported for other chalcogenide-related materials [60,61]. Band gaps of commonly used photovoltaic materials, like CIGS (1.00–1.70 eV) and CdTe (1.45 eV), [62,63] are comparable with those computed here. We can then conclude that the two compounds studied here could be used as one or more of the absorber materials in properly designing tandem solar cells and in general in optoelectronic and photovoltaic devices.

E. Elastic and mechanical properties

The response of a crystalline solid to external forces within the elastic limit can be described by the elastic tensor. This is among the most basic indicators showing the type of interatomic bonding in a particular material and establishes its mechanical stability. In fact, a broad range of mechanical and thermal properties can be derived from the elastic tensor, making it an essential quantity used for screening during the design and discovery of materials [64]. The independent components of the elastic tensor of both KBiSe_2 and NaBiSe_2 in their trigonal structure are reported in Table III. For the trigonal structure, the Born stability criteria at zero pressure require positive diagonal components and the following inequalities to be satisfied: $C_{11} > |C_{12}|$, $C_{44} > 0$, $C_{13}^2 < \frac{1}{2}C_{33}(C_{11} + C_{12})$, and $C_{14}^2 < \frac{1}{2}C_{44}(C_{11} - C_{12}) \equiv C_{44}C_{66}$. These conditions are met for both materials, which must then be considered stable at zero pressure.

The hardness of a compound can be measured by bulk B and shear G moduli, while Young's modulus E describes the stiffness [65]. These parameters are determined from the elastic constants of Table III and are reported in Table IV. When going from KBiSe_2 to NaBiSe_2 E , B , and G all increase, a feature resulting from the smaller ionic radius of Na and the associated smaller volume of NaBiSe_2 . Poisson's ratio ν is often taken as a good measure of whether a material is malleable, and a value > 0.26 is taken as an indication of ductility [66]. Both compounds investigated here are found to be borderline ductile, the Poisson ratio of KBiSe_2 being 0.260 and that of NaBiSe_2 is 0.258. Another indicator of brittleness and ductility of materials is Pugh's ratio (B/G) [67]. In this case, a Pugh ratio of > 1.75 suggests ductility; otherwise, the material is often considered brittle. KBiSe_2 satisfies this con-

TABLE IV. The bulk B , shear G , and Young modulus E (in GPa) of the trigonal structure KBiSe_2 and NaBiSe_2 , together with the Pugh B_H/G_H and Poisson ν ratios. The subscripts v , R , and H describe the Voigt, Reuss, and Hill approximations, respectively.

Mechanical properties	B_v	B_R	B_H	G_v	G_R	G_H	E	B_H/G_H	ν
KBiSe_2	39.79	39.68	39.74	25.05	19.73	22.39	56.55	1.78	0.260
NaBiSe_2	43.97	42.71	43.34	27.11	22.90	25.01	62.92	1.73	0.258

TABLE V. Calculated values of Seebeck coefficients, power factor, and figure of merit (ZT) of KBiSe_2 and NaBiSe_2 with and without SOC, at 300, 450, 600, and 750 K, respectively.

Compounds	Seebeck ($\mu\text{V}/\text{K}$)				Power factor ($\times 10^{10} \text{ W}/\text{mK}^2 \text{ s}$)				Figure of merit (ZT)			
	300 K	450 K	600 K	750 K	300 K	450 K	600 K	750 K	300 K	450 K	600 K	750 K
KBiSe_2												
Without SOC	2045	1394	1070	864	46.30	64.30	78.45	91.42	0.98	0.97	0.93	0.90
With SOC	1355	908	717	600	79.63	116.19	139.78	159.88	0.96	0.91	0.84	0.76
NaBiSe_2												
Without SOC	1975	1379	1055	864	45.00	70.20	89.07	107.93	0.99	0.96	0.93	0.90
With SOC	1232	864	688	585	85.35	133.88	172.80	201.10	0.97	0.90	0.81	0.70

dition with a Pugh ratio of 1.78, while NaBiSe_2 is predicted to be brittle having $B/G = 1.73$.

F. Thermoelectric properties

The figure of merit ZT , electrical conductivity σ , Seebeck coefficient S , and electronic thermal conductivity k_e all measure the performance of thermoelectric materials [68]. A high ZT together with a large Seebeck coefficient as well as electrical conductivity are desired for thermoelectric devices, particularly at moderate temperature. According to earlier work by Nielsen *et al.* [69], compounds with stoichiometry ratio ABX_2 (precisely with group I-V-VI₂) are predicted to have low thermal conductivity but high Seebeck coefficient and electrical conductivity. Note that the Seebeck coefficient can be determined with respect to the n - and p -type carrier concentrations. Peaks in Seebeck coefficient are usually observed between carrier concentrations of 10^{19} and 10^{21} cm^{-3} depending on the nature of the system [70]. Here, the various transport coefficients (Seebeck coefficients, power factor, and figure of merit) are calculated with respect to chemical potential at the PBE and PBE+SOC levels, and their peak values at different temperatures are displayed in Table V. An analysis on their dependence on the carrier concentration is shown in the Supplemental Material [32].

The Seebeck coefficients are presented in Fig. 7 for both compounds in the 300–750 K temperature range. As expected, Seebeck coefficient changes sign when going from n - to

p -type conditions, a transition that, by definition, happens at midgap (the energy zero in the figure is set at the top of the valence band). The highest Seebeck coefficient value is observed for the two compounds at room temperature. For p -type doping at 300 K, KBiSe_2 has its maximum at $2045 \mu\text{V}/\text{K}$, while that of NaBiSe_2 is at $1975 \mu\text{V}/\text{K}$ (PBE values). In the n -type side of the doping, the Seebeck coefficient at the same temperature reaches up to $1830 \mu\text{V}/\text{K}$ for KBiSe_2 and $1737 \mu\text{V}/\text{K}$ for NaBiSe_2 (PBE values). Due to the presence of the Se and Bi heavy ions, the influence of SOC has also been considered in these calculations. Upon introducing SOC, the Seebeck coefficients show a remarkable decrease of $\sim 35\%$ for both compounds at all temperatures (see Table V). This trend agrees with previously reported evidence for other chalcogenide-related materials [71,72]. Note that both the PBE and PBE+SOC Seebeck coefficient peak values obtained at room temperature are >210.46 and $178.95 \mu\text{V}/\text{K}$, the values reported for Bi_2Te_3 , a common thermoelectric material [18]. This demonstrates that the two compounds investigated are promising for thermoelectric applications in both doping conditions.

Figures S2(a) and S2(b) in the Supplemental Material [32] present plots of the Seebeck coefficient as a function of the charge-carrier concentration for KBiSe_2 and NaBiSe_2 at different temperatures (300, 450, 600, and 750 K). In general, an increase in hole concentration produces a reduction in the Seebeck coefficient at all temperatures for both materials. In

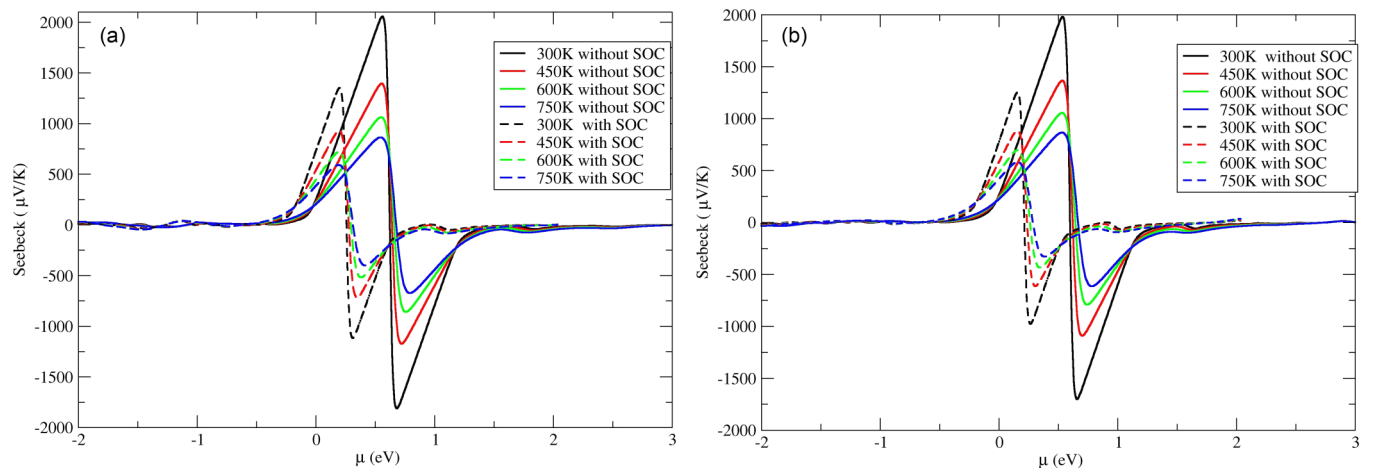


FIG. 7. Seebeck coefficient of (a) KBiSe_2 and (b) NaBiSe_2 as a function of the chemical potential μ computed at the PBE level with and without spin-orbit coupling (SOC). The energy zero is placed at the top of the valence band.

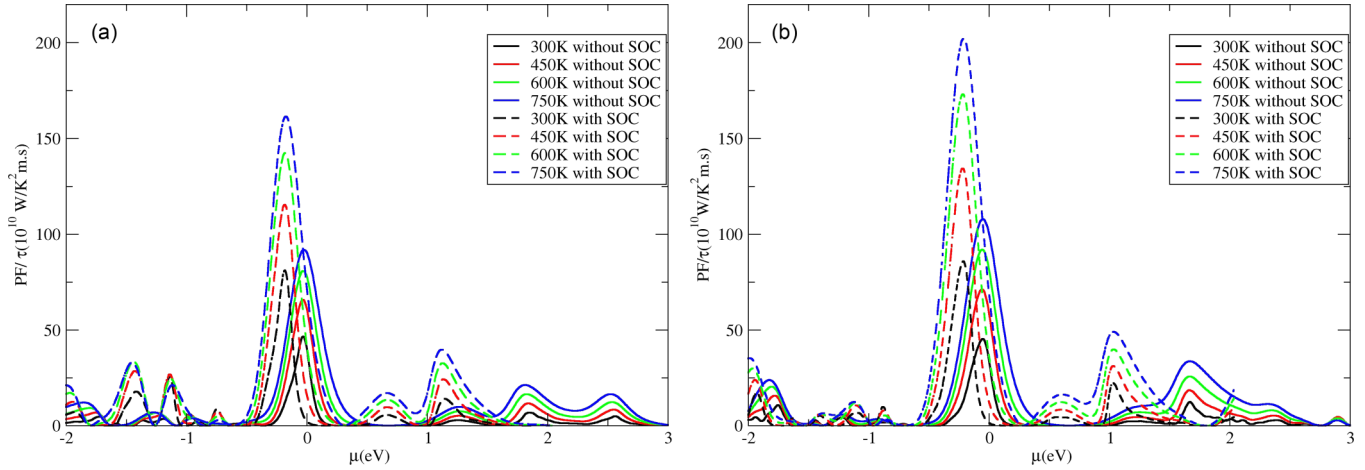


FIG. 8. Power factor of (a) KBiSe_2 and (b) NaBiSe_2 as a function of the chemical potential μ computed at the PBE level with and without spin-orbit coupling (SOC). The energy zero is placed at the top of the valence band.

contrast, in n -type conditions, the Seebeck coefficient gets larger as the carrier concentration increases. As a reference, at room temperature and a carrier concentration of 10^{19} cm^{-3} , the Seebeck coefficient is computed as $\sim 562 \mu\text{V/K}$ for KBiSe_2 and $520 \mu\text{V/K}$ for NaBiSe_2 for p -type transport. These Seebeck coefficient values for both compounds at room temperature with respect to carrier concentration are higher than those commonly reported for high-performance thermoelectric materials. For instance, Bi_2Te_3 , known for its improved performance in portable/wearable electronic due to its thermoelectric properties, displays $S = 313 \mu\text{V/K}$ for p -type conduction [73], indicating that the ABiSe_2 family may have potential for thermoelectric applications. In addition, a recent report has shown that using deposition temperatures of 300, 400, and 450 °C, Bi_2Te_3 exhibits Seebeck coefficients of 196.4, 193.5, and 135.7 $\mu\text{V/K}$, respectively [74]. Therefore, because of the outstanding Seebeck coefficient of ABiSe_2 when compared with that of Bi_2Te_3 , it is expected that this class of materials can also be identified as potential candidates for wearable thermoelectric devices.

The power factor of the two compounds increases with an increase in temperature, as displayed in Figs. 8(a) and 8(b). At around zero chemical potential, the highest power factor is observed for the two systems, a feature that implies a high figure of merit in this region. In addition, it is noted that the power factor of both systems goes to ~ 0 at ~ 0.50 and 0.90 eV, respectively, for KBiSe_2 and NaBiSe_2 . This is where the electrical conductivity vanishes. Again, at room temperature, KBiSe_2 possesses a power factor of $\sim 46.3 \times 10^{10} \text{ W/mK}^2 \text{ s}$ (PBE value), a value higher than that of NaBiSe_2 having $45 \times 10^{10} \text{ W/mK}^2 \text{ s}$ at zero chemical potential (these are all in units of the relaxation time τ). When SOC is included in the calculation, this results in a remarkable increase in the thermoelectric power factor, which roughly doubles with respect to the PBE values. At room temperature, the PBE+SOC peak values are 79×10^{10} and $85.35 \times 10^{10} \text{ W/mK}^2 \text{ s}$ for KBiSe_2 and NaBiSe_2 , respectively. Similar trends have been reported in a study by Bera *et al.* [75]. It is worth noting that the peak values of the power factors obtained for PBE (PBE+SOC) at room temperature (300 K) are $> 13.2 \times 10^{10} \text{ W/mK}^2 \text{ s}$ ($25.91 \times 10^{10} \text{ W/mK}^2 \text{ s}$) of HfSe_2 ,

which has been reported to be an excellent thermoelectric material [75].

The calculated power factors with respect to the carrier concentration at various temperatures for p - and n -type doping conditions are presented in Figs. S3(a) and S3(b) in the Supplemental Material [32]. It is observed that the power factor increases with raising the carrier concentration and attains its maximum values at 10^{21} cm^{-3} carrier concentration. This falls within the carrier concentration range where typical semiconducting materials exhibit better performance [68]. The values obtained at room temperature for this carrier concentration (10^{21} cm^{-3}) are 11.67×10^{10} and $44.99 \times 10^{10} \text{ W/mK}^2 \text{ s}$ for n - and p -type NaBiSe_2 , while KBiSe_2 has its peaks at 6.47×10^{10} and $46.14 \times 10^{10} \text{ W/mK}^2 \text{ s}$ for n - and p -type doping, respectively. The maximum power factors for both n - and p -type conditions are the consequence of the high Seebeck value and electrical conductivity.

Finally, the efficiency of the thermoelectric devices can be assessed by computing the figure of merit ZT , a quantity directly proportional to the temperature, Seebeck coefficient, and electrical conductivity and inversely proportional to the thermal conductivity. Materials with ZT values of about unity or greater are considered suitable for thermoelectric devices [76,77]. As one can appreciate in Figs. 9(a) and 9(b), ZT 's against chemical potential plots for KBiSe_2 and NaBiSe_2 show approximately the same behavior. Here, ZT reaches a value close to unity (with values of 0.98 for KBiSe_2 and 0.99 for NaBiSe_2) at room temperature and gets slightly reduced as the temperature increases (PBE results). Furthermore, it is observed that the PBE-computed ZT rises sharply as the chemical potential increases from zero, with the maximum values noticed at ~ 0.50 and 0.70 eV for KBiSe_2 and NaBiSe_2 , respectively. Upon the introduction of SOC, ZT does not change significantly for both systems, as seen in Fig. 9 and Table V. This is due to the notable increase in the power factor of both compounds calculated in this work. Here, ZT attains values approaching unity (0.96 for KBiSe_2 and 0.97 for NaBiSe_2) at standard room temperature and experiences a slight decrease as the temperature rises. A slight shift and reduction are noticed in the chemical potential at the inclusion

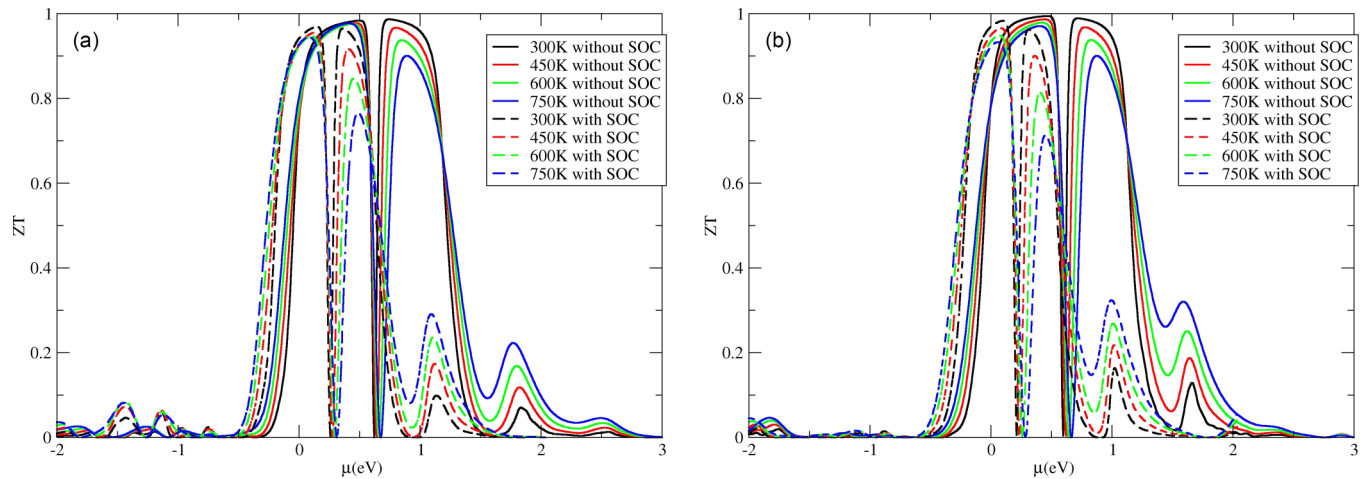


FIG. 9. Figure of merit of (a) KBiSe_2 and (b) NaBiSe_2 as a function of the chemical potential μ computed at the PBE level with and without spin-orbit coupling (SOC). The energy zero is placed at the top of the valence band.

of SOC, a factor we attribute to reduced band gap observed when SOC was considered. Since devices capable of supplying an input power to numerous sensors, electronic and wearable devices in a temperature range $\sim 300\text{--}400$ K are highly sought after [70], it is safe to suggest that the class of thermoelectric materials reported in this work has useful characteristics for making flexible thermoelectric powering devices due to their nontoxic composition, figure of merit of approximately unity at low temperature, and their ductile nature.

IV. CONCLUSIONS

In summary, the structural, electronic, and mechanical properties of KBiSe_2 and NaBiSe_2 have been computed by using first-principles methods together with an analysis of their dynamical and thermodynamic stability. The trigonal structure of KBiSe_2 previously synthesized [27] has been obtained from the Crystallography Open Database, while NaBiSe_2 has been modeled by exchanging K with Na at the corresponding A cation site. For KBiSe_2 , the calculated lattice parameters are in good agreement with experimental data, while no information is available for trigonal NaBiSe_2 . The calculations then reveal that the two compounds are structurally very similar, except for the cell volume, a feature mainly due to the different atomic radius of the alkali metals involved.

The electronic properties computed at the HSE06 (PBE) level return band gaps of 1.96 eV (1.26 eV) for KBiSe_2 and 1.93 eV (1.25 eV) for NaBiSe_2 . This is significantly higher than the observed optical gap of KBiSe_2 at room temperature. However, the inclusion of SOC and temperature corrections brings the HSE06+SOC values to 1.20 eV (KBiSe_2) and 1.13 eV (NaBiSe_2), values much more in line with experimental evidence. Furthermore, SOC impacted the dielectric functions with a change in the energy range along the peak position for both compounds. This is also evident in the transport coefficients of the thermoelectric properties results when SOC was considered. It is worth noting that materials with an absorption onset between 0.80 and 1.70 eV are considered suitable for solar cell applications [58], and this was noticed

in the optical properties results of the materials computed in this work with absorption onset values of 1.50 and 0.85 eV for both PBE and PBE+SOC functionals, respectively. With these results in hand and the computed components of the dielectric function, we can conclude that both KBiSe_2 and NaBiSe_2 appear promising as light-absorbing materials in the visible light range. The dynamical, thermodynamic, and mechanical properties of both systems suggest that they are stable. In addition, it is found that this class of materials with and without SOC has a high Seebeck coefficient, with values greater than that of typical high-performing thermoelectric compounds such as Bi_2Te_3 [73]. As such, we can conclude that both KBiSe_2 and NaBiSe_2 have potential in photovoltaic and thermoelectric applications.

ACKNOWLEDGMENTS

The authors acknowledge Atlantic Technological University, Sligo, President Bursary Award under the Grant No. PPRES089 for financial assistance granted to SAA. SBA appreciates the Modelling & Computation for Health and Society (MOCHAS) Group of Atlantic Technological University, Ireland, for financial support. The funding support of the Irish Research Council granted to DOO with Project ID GOIPD/2021/28 is also acknowledged. SS thanks additional financial support from the Irish Research Council (IRCLA/2019/127). FE would like to acknowledge the NOMDEE project funded by the Qatar Environment and Energy Research Institute and the AIPAM Project No. VPR-TG01-006 funded by the office of Hamad Bin Khalifa University (HBKU) Vice President of Research. The Trinity Centre for High Performance Computing Kelvin cluster was used for most of these calculations (Project codes: HPC_21_01219, HPC_22_01290 and HPC_22_01254). This cluster was supported by funding from the Higher Education Authority's PRTLI program. The Irish Centre for High-End Computing (Project codes: isphy006c, atphy001c and isphy005c) is also acknowledged by the authors for providing computing resources.

- [1] Q. Tai, K.-C. Tang, and F. Yan, Recent progress of inorganic perovskite solar cells, *Energy Environ. Sci.* **12**, 2375 (2019).
- [2] T. I. Al-Muhimeed, A. Shafique, A. A. AlObaid, M. Morsi, G. Nazir, M. mana AL-Anazy, and Q. Mahmood, New lead-free double perovskites $X_2\text{GeI}_6$ ($X = \text{K}, \text{Rb}, \text{Cs}$) for solar cells, and renewable energy as an alternate of hybrid perovskites, *Int. J. Energy Res.* **45**, 19645 (2021).
- [3] F. Cao, P. Zhang, and L. Li, Multidimensional perovskite solar cells, *Fundam. Res.* **2**, 237 (2022).
- [4] J. Jeong, M. Kim, J. Seo, H. Lu, P. Ahlawat, A. Mishra, Y. Yang, M. A. Hope, F. T. Eickemeyer, and M. Kim, Pseudohalide anion engineering for α -FAPbI₃ perovskite solar cells, *Nature (London)* **592**, 381 (2021).
- [5] Y.-Y. Zhang, S. Chen, P. Xu, H. Xiang, X.-G. Gong, A. Walsh, and S.-H. Wei, Intrinsic instability of the hybrid halide perovskite semiconductor $\text{CH}_3\text{NH}_3\text{PbI}_3$, *Chin. Phys. Lett.* **35**, 036104 (2018).
- [6] L. Xiang, F. Gao, Y. Cao, D. Li, Q. Liu, H. Liu, and S. Li, Progress on the stability and encapsulation techniques of perovskite solar cells, *Org. Electron.* **106**, 106515 (2022).
- [7] N. K. Noel, S. D. Stranks, A. Abate, C. Wehrenfennig, S. Guarnera, A.-A. Haghighirad, A. Sadhanala, G. E. Eperon, S. K. Pathak, and M. B. Johnston, Lead-free organic-inorganic tin halide perovskites for photovoltaic applications, *Energy Environ. Sci.* **7**, 3061 (2014).
- [8] S. Aina, B. Villacampa, and M. Bernechea, Earth-abundant nontoxic perovskite nanocrystals for solution processed solar cells, *Mater. Adv.* **2**, 4140 (2021).
- [9] J. F. Khoury, B. Han, M. Jovanovic, R. Singha, X. Song, R. Queiroz, N.-P. Ong, and L. M. Schoop, A class of magnetic topological material candidates with hypervalent Bi chains, *J. Am. Chem. Soc.* **144**, 9785 (2022).
- [10] S. F. Hoeffler, G. Trimmel, and T. Rath, Progress on lead-free metal halide perovskites for photovoltaic applications: A review, *Monatsh. Chem.* **148**, 795 (2017).
- [11] O. A. Lozhkina, A. A. Murashkina, V. V. Shilovskikh, Y. V. Kapitonov, V. K. Ryabchuk, A. V. Emeline, and T. Miyasaka, Invalidation of band-gap engineering concept for Bi^{3+} heterovalent doping in CsPbBr_3 halide perovskite, *J. Phys. Chem. Lett.* **9**, 5408 (2018).
- [12] Z. Liu and F. Yan, The application of bismuth-based oxides in organic-inorganic hybrid photovoltaic devices, *J. Am. Ceram. Soc.* **95**, 1944 (2012).
- [13] I. S. Khare, N. J. Szymanski, D. Gall, and R. E. Irving, Electronic, optical, and thermoelectric properties of sodium pnictogen chalcogenides: A first principles study, *Comput. Mater. Sci.* **183**, 109818 (2020).
- [14] M.-A. Shahbazi, L. Faghfoury, M. P. Ferreira, P. Figueiredo, H. Maleki, F. Sefat, J. Hirvonen, and H. A. Santos, The versatile biomedical applications of bismuth-based nanoparticles and composites: Therapeutic, diagnostic, biosensing, and regenerative properties, *Chem. Soc. Rev.* **49**, 1253 (2020).
- [15] C. Yang, Z. Wang, Y. Wu, Y. Lv, B. Zhou, and W.-H. Zhang, Synthesis, characterization, and photodetector application of alkali metal bismuth chalcogenide nanocrystals, *ACS Appl. Energy Mater.* **2**, 182 (2018).
- [16] B. A. Rosales, M. A. White, and J. Vela, Solution-grown sodium bismuth dichalcogenides: Toward earth-abundant, biocompatible semiconductors, *J. Am. Chem. Soc.* **140**, 3736 (2018).
- [17] S. K. R., A. Akande, F. El-Mellouhi, H. Park, and S. Sanvito, Theoretical investigation of the structural, elastic, electronic, and dielectric properties of alkali-metal-based bismuth ternary chalcogenides, *Phys. Rev. Mater.* **4**, 075401 (2020).
- [18] M. Z. Mohyedin, M. F. M. Taib, A. Radzwan, A. Shaari, M. Mustafa, B. U. Haq, and M. Z. A. Yahya, First principles study of the effect of spin-orbit coupling on thermoelectric properties of bismuth telluride, *Comput. Theor. Chem.* **1182**, 112851 (2020).
- [19] J. Baker, R. S. Kumar, D. Sneed, A. Connolly, Y. Zhang, N. Velisavljevic, J. Paladugu, M. Pravica, C. Chen, and A. Cornelius, Pressure induced structural transitions in CuSbS_2 and CuSbSe_2 thermoelectric compounds, *J. Alloys Compd.* **643**, 186 (2015).
- [20] C. Lee, S. Kim, W.-J. Son, J.-H. Shim, and M.-H. Whangbo, Ternary selenides $\text{A}_2\text{Sb}_4\text{Se}_8$ ($A = \text{K}, \text{Rb}$ and Cs) as an n -type thermoelectric material with high power factor and low lattice thermal conductivity: Importance of the conformationally flexible Sb–Se–Se–Sb bridges, *RSC Adv.* **10**, 14415 (2020).
- [21] A. Tabeti, M. Batouche, K. Bidai, A. Djied, T. Seddik, R. Khenata, H. Baltach, and X. Wang, DFT investigation on the electronic and thermoelectric properties of ternary semiconductor AgBiS_2 for energy conversion application, *Chin. J. Phys.* **59**, 578 (2019).
- [22] H.-J. Wu, P.-C. Wei, H.-Y. Cheng, J.-R. Deng, and Y.-Y. Chen, Ultralow thermal conductivity in n -type Ge-doped AgBiSe_2 thermoelectric materials, *Acta Mater.* **141**, 217 (2017).
- [23] Y. Goto, A. Nishida, H. Nishiata, M. Murata, C. H. Lee, A. Miura, C. Moriyoshi, Y. Kuroiwa, and Y. Mizuguchi, Effect of Te substitution on crystal structure and transport properties of AgBiSe_2 thermoelectric material, *Dalton Trans.* **47**, 2575 (2018).
- [24] P. H. Le, S.-P. Chiu, S.-R. Jian, C. W. Luo, J.-Y. Lin, J.-J. Lin, K. H. Wu, and M. Gospodinov, Nanomechanical, structural, and transport properties of $\text{Bi}_3\text{Se}_2\text{Te}$ thin films, *J. Alloys Compd.* **679**, 350 (2016).
- [25] H. Zhu, J.-Y. Zhao, and C. Xiao, Improved thermoelectric performance in n -type BiTe facilitated by defect engineering, *Rare Met.* **40**, 2829 (2021).
- [26] J. Qiao, Y. Zhao, Q. Jin, J. Tan, S. Kang, J. Qiu, and K. Tai, Tailoring nanoporous structures in Bi_2Te_3 thin films for improved thermoelectric performance, *ACS Appl. Mater. Interfaces* **11**, 38075 (2019).
- [27] R. McClain, C. D. Malliakas, J. Shen, J. He, C. Wolverton, G. B. González, and M. G. Kanatzidis, Mechanistic insight of KBiQ_2 ($Q = \text{S}, \text{Se}$) using panoramic synthesis towards synthesis-by-design, *Chem. Sci.* **12**, 1378 (2021).
- [28] G. Kresse and J. Furthmüller, Efficient iterative schemes for *ab initio* total-energy calculations using a plane-wave basis set, *Phys. Rev. B* **54**, 11169 (1996).
- [29] J. P. Perdew, J. A. Chevary, S. H. Vosko, K. A. Jackson, M. R. Pederson, D. J. Singh, and C. Fiolhais, Atoms, molecules, solids, and surfaces: Applications of the generalized gradient approximation for exchange and correlation, *Phys. Rev. B* **46**, 6671 (1992).
- [30] G. Kresse and D. Joubert, From ultrasoft pseudopotentials to the projector augmented-wave method, *Phys. Rev. B* **59**, 1758 (1999).
- [31] P. E. Blöchl, Projector augmented-wave method, *Phys. Rev. B* **50**, 17953 (1994).

- [32] See Supplemental Material at <http://link.aps.org/supplemental/10.1103/PhysRevMaterials.8.015404> for HSE06-calculated energy band structure, Seebeck coefficient and Power factor against carrier concentration for the two compounds. It also includes K-points convergence during structure optimization, molecular dynamics PBE-calculated band structures of KBiSe₂ at the temperature in the range of 100 K-500 K and temperature fluctuations with respect to the AIMD steps of KBiSe₂ heated to the target temperature of 300 K at 4 fs.
- [33] S. Grimme, S. Ehrlich, and L. Goerigk, Effect of the damping function in dispersion corrected density functional theory, *J. Comput. Chem.* **32**, 1456 (2011).
- [34] S. Grimme, J. Antony, S. Ehrlich, and H. Krieg, A consistent and accurate *ab initio* parametrization of density functional dispersion correction (DFT-D) for the 94 elements H-Pu, *J. Chem. Phys.* **132**, 154104 (2010).
- [35] R. R. Pela, M. Marques, and L. K. Teles, Comparing LDA-1/2, HSE03, HSE06 and G0W0 approaches for band gap calculations of alloys, *J. Phys. Condens. Matter* **27**, 505502 (2015).
- [36] S. Nosé, A unified formulation of the constant temperature molecular dynamics methods, *J. Chem. Phys.* **81**, 511 (1984).
- [37] S. Nosé, A molecular dynamics method for simulations in the canonical ensemble, *Mol. Phys.* **52**, 255 (1984).
- [38] B. Fultz, Vibrational thermodynamics of materials, *Prog. Mater. Sci.* **55**, 247 (2010).
- [39] W. Qian and C. Zhang, Review of the phonon calculations for energetic crystals and their applications, *Energ. Mater. Front.* **2**, 154 (2021).
- [40] A. Togo and I. Tanaka, First principles phonon calculations in materials science, *Scr. Mater.* **108**, 1 (2015).
- [41] V. B. Bobrov and S. A. Trigger, Kramers-Kronig relations for the dielectric permittivity of the Coulomb system with a single-species Bose-Einstein condensate, *J. Low Temp. Phys.* **200**, 118 (2020).
- [42] A. Bafekry, M. Faraji, M. M. Fadlallah, H. R. Jappor, N. N. Hieu, M. Ghergherehchi, S. A. H. Feghhi, and D. Gogova, Prediction of two-dimensional bismuth-based chalcogenides Bi₂X₃ (X = S, Se, Te) monolayers with orthorhombic structure: A first-principles study, *J. Phys. D: Appl. Phys.* **54**, 395103 (2021).
- [43] S. M. Rogge, M. Waroquier, and V. Van Speybroeck, Reliably modeling the mechanical stability of rigid and flexible metal-organic frameworks, *Acc. Chem. Res.* **51**, 138 (2018).
- [44] F. Mouhat and F.-X. Coudert, Necessary and sufficient elastic stability conditions in various crystal systems, *Phys. Rev. B* **90**, 224104 (2014).
- [45] G. K. Madsen and D. J. Singh, BoltzTraP. A code for calculating band-structure dependent quantities, *Comput. Phys. Commun.* **175**, 67 (2006).
- [46] M. Rouzbehi, A. Kazempour, A. Shokri, L. Gholamzadeh, and F. Golami, Pressure induced renormalization of thermal conductivity of uranium nitride: A first principles study, *Physica B* **572**, 230 (2019).
- [47] S. Curtarolo, W. Setyawan, G. L. Hart, M. Jahnatek, R. V. Chepulskii, R. H. Taylor, S. Wang, J. Xue, K. Yang, and O. Levy, AFLOW: An automatic framework for high-throughput materials discovery, *Comput. Mater. Sci.* **58**, 218 (2012).
- [48] A. Jain, S. P. Ong, G. Hautier, W. Chen, W. D. Richards, S. Dacek, S. Cholia, D. Gunter, D. Skinner, and G. Ceder, Commentary: The Materials Project: A materials genome approach to accelerating materials innovation, *APL Mater.* **1**, 011002 (2013).
- [49] K. Qu, H. Bale, Z. W. Riedel, J. Park, L. Yin, A. Schleife, and D. P. Shoemaker, Morphology and growth habit of the new flux-grown layered semiconductor KBiS₂ revealed by diffraction contrast tomography, *Cryst. Growth Des.* **22**, 3228 (2022).
- [50] J. Ning, L. Zheng, W. Lei, S. Wang, J. Xi, and J. Yang, Temperature-dependence of the band gap in the all-inorganic perovskite CsPbI₃ from room to high temperatures, *Phys. Chem. Chem. Phys.* **24**, 16003 (2022).
- [51] D. O. Obada, S. A. Abolade, S. K. R., A. M. Ukpong, and A. Akande, *Ab initio* calculations of the properties of defective CsSnCl₃: The role of anion-cation pair defect, *Solid State Ionics* **399**, 116262 (2023).
- [52] F. Parvin and S. H. Naqib, Structural, elastic, electronic, thermodynamic, and optical properties of layered BaPd₂As₂ pnictide superconductor: A first principles investigation, *J. Alloys Compd.* **780**, 452 (2019).
- [53] S. K. Mitro, M. A. Hadi, F. Parvin, R. Majumder, S. H. Naqib, and A. Islama, Effect of boron incorporation into the carbon-site in Nb₂SC MAX phase: Insights from DFT, *J. Mater. Res. Technol.* **11**, 1969 (2021).
- [54] M. Rasheduzzaman, K. M. Hossain, S. K. Mitro, M. A. Hadi, J. K. Modak, and M. Z. Hasan, Structural, mechanical, thermal, and optical properties of inverse-Heusler alloys Cr₂CoZ (Z = Al, In): A first-principles investigation, *Phys. Lett. A* **385**, 126967 (2021).
- [55] N. P. Raju and R. Thangavel, Theoretical investigation of spin-orbit coupling on structural, electronic and optical properties for CuAB₂ (A = Sb, Bi; B = S, Se) compounds using Tran-Blaha-modified Becke-Johnson method: A first-principles approach, *J. Alloys Compd.* **830**, 154621 (2020).
- [56] H. Ni, M. Li, Y. Hu, C. Mao, L. Xue, H. Zeng, Z. Yan, Y. Wu, and C. Zheng, Two-dimensional SnSe/GeSe van der Waals heterostructure with strain-tunable electronic and optical properties, *J. Phys. Chem. Solids* **131**, 223 (2019).
- [57] N. J. Szymanski, L. N. Walters, O. Hellman, D. Gall, and S. V. Khare, Dynamical stabilization in delafossite nitrides for solar energy conversion, *J. Mater. Chem. A* **6**, 20852 (2018).
- [58] S. Ruhle, A. Y. Anderson, H.-N. Barad, B. Kupfer, Y. Bouhadana, E. Rosh-Hodesh, and A. Zaban, All-oxide photovoltaics, *J. Phys. Chem. Lett.* **3**, 3755 (2012).
- [59] J.-L. Bredas, Mind the gap! *Mater. Horizons* **1**, 17 (2014).
- [60] E. A. Moujaes and A. C. Dias, On the excitonic effects of the 1T and 1OT phases of PdS₂, PdSe₂, and PdSSe monolayers, *J. Phys. Chem. Solids* **182**, 111573 (2023).
- [61] A. Lawal, A. Shaari, R. Ahmed, and N. Jarkoni, Sb₂Te₃ crystal a potential absorber material for broadband photodetector: A first-principles study, *Results Phys.* **7**, 2302 (2017).
- [62] T. Tinoco, C. Rincón, M. Quintero, and G. S. Pérez, Phase diagram and optical energy gaps for CuInyGa_{1-y}Se₂ alloys, *Phys. Status Solidi A* **124**, 427 (1991).
- [63] D. A. Jenny and R. H. Bube, Semiconducting cadmium telluride, *Phys. Rev.* **96**, 1190 (1954).
- [64] M. De Jong, W. Chen, T. Angsten, A. Jain, R. Notestine, A. Gamst, M. Sluiter, C. Krishna Ande, S. van der Zwaag, J. J. Plata *et al.*, Charting the complete elastic properties of inorganic crystalline compounds, *Sci. Data* **2**, 150009 (2015).
- [65] H. Koç, A. M. Mamedov, E. Deligoz, and H. Ozisik, First principles prediction of the elastic, electronic, and optical properties

- of Sb_2S_3 and Sb_2Se_3 compounds, *Solid State Sci.* **14**, 1211 (2012).
- [66] S. Chen, Y. Sun, Y.-H. Duan, B. Huang, and M.-J. Peng, Phase stability, structural and elastic properties of C15-type Laves transition-metal compounds MCo_2 from first-principles calculations, *J. Alloys Compd.* **630**, 202 (2015).
- [67] S. F. Pugh, XCII. Relations between the elastic moduli and the plastic properties of polycrystalline pure metals, *Philos. Mag.* **45**, 823 (1954).
- [68] H. S. Kim, W. Liu, G. Chen, C.-W. Chu, and Z. Ren, Relationship between thermoelectric figure of merit and energy conversion efficiency, *Proc. Natl. Acad. Sci. USA* **112**, 8205 (2015).
- [69] M. D. Nielsen, V. Ozolins, and J. P. Heremans, Lone pair electrons minimize lattice thermal conductivity, *Energy Environ. Sci.* **6**, 570 (2013).
- [70] G. J. Snyder and E. S. Toberer, Complex thermoelectric materials, *Nat. Mater.* **7**, 105 (2008).
- [71] L. Wu, J. Yang, S. Wang, P. Wei, J. Yang, W. Zhang, and L. Chen, Two-dimensional thermoelectrics with Rashba spin-split bands in bulk BiTeI , *Phys. Rev. B* **90**, 195210 (2014).
- [72] S.-D. Guo and J.-L. Wang, Spin-orbital coupling effect on the power factor in semiconducting transition-metal dichalcogenide monolayers, *Semicond. Sci. Technol.* **31**, 095011 (2016).
- [73] S. K. Mishra, S. Satpathy, and O. Jepsen, Electronic structure and thermoelectric properties of bismuth telluride and bismuth selenide, *J. Phys. Condens. Matter* **9**, 461 (1997).
- [74] Q. Zou, H. Shang, D. Huang, B. Xie, L. Zhang, K. Wang, H. Dong, C. Li, H. Gu, and F. Ding, Bi_2Te_3 -based flexible thermoelectric generator for wearable electronics, *Appl. Phys. Lett.* **120**, 023903 (2022).
- [75] J. Bera, A. Betal, and S. Sahu, Spin orbit coupling induced enhancement of thermoelectric performance of HfX_2 ($X = \text{S}, \text{Se}$) and its Janus monolayer, *J. Alloys Compd.* **872**, 159704 (2021).
- [76] O. Rabina, Y.-M. Lin, and M. S. Dresselhaus, Anomalously high thermoelectric figure of merit in $\text{Bi}_{1-x}\text{Sb}_x$ nanowires by carrier pocket alignment, *Appl. Phys. Lett.* **79**, 81 (2001).
- [77] T. Takeuchi, Conditions of electronic structure to obtain large dimensionless figure of merit for developing practical thermoelectric materials, *Mater. Trans.* **50**, 2359 (2009).